REVISION 1

Sub-Micron-Scale Spatial Heterogeneity in Silicate Glasses Using Aberration-Corrected Scanning Transmission Electron Microscopy

Katherine D. Burgess[1], Rhonda M. Stroud[2], M. Darby Dyar[3], and Molly C. McCanta[4]

[1]ASEE Postdoctoral Fellow, U.S. Naval Research Laboratory, Washington, DC 20375 (kate.burgess.ctr@nrl.navy.mil)

[2]U.S. Naval Research Laboratory, Washington, DC 20375

[3]Mount Holyoke College, South Hadley, MA 01075

[4]Tufts University, Medford, MA 02155

Abstract

Experimental silicate glasses are often used as analog and calibration material for terrestrial and planetary materials. Measurements of Fe oxidation state using electron energy loss spectroscopy (EELS) in an aberration-corrected scanning transmission electron microscope (ac-STEM) show that a suite of experimental silicate (e.g., basaltic, andesitic, rhyolitic) glasses have spatially heterogeneous oxidation states at scales of 10s of nanometers. Nano-crystals are observed in several of the glasses, indicating nucleation and incipient crystallization not seen at the scale of electron microprobe analysis (EMPA). Glasses prepared in air are uniformly oxidized while glasses prepared at the iron-wustite (IW) or quartz-fayalite-magnetite (QFM) buffers range from reduced to highly oxidized. EELS spectral shapes indicate that oxidized glasses have tetrahedral Fe^{3+}. The nano-scale compositional and structural heterogeneities present in the experimental glasses mean that the suitability of such glasses as analogs for natural materials and calibration standards depends strongly on the scale of the measurements being done. The electron beam quickly damages silicate glass, but data showing changes in oxidation

state among and within samples can be obtained with careful control of the beam current and dwell time. Determination of oxidation state in silicate glasses via STEM-EELS is very challenging, and accurate and reliable measurements of $Fe^{3+}/\Sigma Fe$ require careful sample preparation and control of microscope conditions and benefit from comparison to complementary techniques.

Keywords: iron oxidation; silicate glass; transmission electron microscopy (TEM); electron energy loss spectroscopy (EELS); beam damage

Introduction

Motivation

Nano-scale measurements of terrestrial and planetary materials can provide unique information about formation and alteration processes. Variations in structure and chemistry at this scale are inherent to some alteration processes and important in dynamics of initial crystallization and phase changes. Micro-X-ray absorption near-edge spectroscopy (μ-XANES) has been used to map redox and speciation of Fe at ~10 μm scales in a variety of minerals, glasses, and metamorphic rocks (Dyar et al., 2002; Dyar et al., 2016a; Dyar et al., 2016b; Muñoz et al., 2006), while scanning transmission X-ray microscopy (STXM) has been used to map $Fe^{3+}/\Sigma Fe$ at finer spatial scales (~20 nm) (Bourdelle et al., 2013a; Bourdelle et al., 2013b; Elmaleh et al., 2015; Le Guillou et al., 2015). Energy-filtered imaging in conventional transmission electron microscopy (EFTEM) has also been used to map changes in valence state with a spatial resolution of a few nanometers (Golla and Putnis, 2001). For example, the nano-scale analyses of Fe oxidation state lend insights to studies of aqueous alteration processes in CAIs in carbonaceous chondrites (Elmaleh et al., 2015), alteration during capture of comet Wild 2 grains and variability in precursor phases for Stardust tracks (Stodolna et al., 2013), and Fe^{2+}

and Fe^{3+} partitioning behavior in diamond anvil cell experiments (Prescher et al., 2014). The development of electron energy-loss spectroscopy (EELS) in the aberration-corrected scanning transmission electron microscope (ac-STEM) is leading to significant improvement in both the spatial and energy resolution available for the analysis of such materials, as illustrated by recent measurements of nano-phase Fe-rich grains in space-weathered rims of lunar soil showing that individual Fe particles can vary significantly in their level of oxidation (Thompson et al., 2016).

The present work illustrates both the power and challenges of using very-high resolution, sub-nanometer analysis techniques to relate bulk material properties to nano-scale features. The homogeneity of silicate glasses at the micrometer-scale make them ideal for many characterization methods with beam sizes down to ~1 μm, but the non-random structure and compositional variations at smaller length scales becomes apparent in STEM measurements. Additionally, sensitivity to the electron beam leads to changes in composition and oxidation state that can be difficult to detangle from the inherent variability of the glass. Even so, EELS and EDS measurements in silicate glasses enable detection of nano-crystals and dynamic changes in glass structure not seen by other means.

Background

Synthetic and experimentally-equilibrated glasses are among the standards used in many analytical techniques and are generally confirmed to be homogenous at the scales of the measurements for which they are used. While glasses lack the long-range order seen in crystals, measurements of the short- and medium-range ordering up to ~1-2 nm in silicate glasses show that glasses are not always random mixtures of components and structurally and can be quite varied (Mysen and Richet, 2005). Short-range order in silicate melts and glasses, encompassing nearest-neighbors and ion coordination, closely resembles that of crystalline silicates, with

networks of SiO_4-tetrahedra in which Si^{4+} may be replaced by cations of similar ionic radius and charge (e.g., Al^{3+}, Fe^{3+}, Ti^{4+}, P^{5+}). Intermediate- or medium-range order, which includes the arrangement of the tetrahedral structural units such as in rings, chains, and sheets, has been shown to depend on quench rate and composition (Stebbins, 1987, 1988; Virgo et al., 1980). Other cations in the glass serve to either charge balance tetrahedra or as network-modifiers and may show preference for bonding to specific types of tetrahedral units (Lee et al., 2003; Lee et al., 2005). The ordering of the constitutive structural units and inherent non-randomness of melts and glasses is important in volume nucleation (Deubener, 2005).

Measurements of $Fe^{3+}/\Sigma Fe$ in terrestrial and planetary materials have been carried out using a variety of measurement techniques that sample materials at a range of spatial scales. In order of decreasing sample size, these include wet chemical methods (e.g., Christie et al., 1986), Mössbauer spectroscopy (e.g., Bancroft et al., 1967; Jayasuriya et al., 2004), x-ray absorption spectroscopy (XAS) (e.g., Bajt et al., 1994; Cottrell and Kelley, 2011; Dyar et al., 1998; Dyar et al., 2016b), electron microprobe (e.g., Herd et al., 2001), Raman (e.g., Roskosz et al., 2008), and EELS or EFTEM (e.g., Garvie and Buseck, 1998; Golla and Putnis, 2001; Van Aken et al., 1998; Van Aken and Liebscher, 2002). Of these techniques, EELS in a TEM provides the highest spatial resolution, and thus the best chance of observing fine-scale variations due to structural changes. It is unclear how the non-random structure of glasses and possible preferential bonding to specific structural units is exhibited in $Fe^{3+}/\Sigma Fe$ at sub-nanometer scales, although there is evidence of Fe clustering depending on coordination and possibly valence (Weigel et al., 2008). Quench rate affects both the iron valence and coordination in glasses (Dyar, 1984; Dyar and Birnie, 1984) in addition to the over-all glass structure (Stebbins, 1988), suggesting that local variations in $Fe^{3+}/\Sigma Fe$ can occur.

When EELS is used as part of a STEM, in which a highly-focused electron beam is rastered across a portion of the sample, very-high-resolution images are obtained at the atom-scale. The combination of spatially resolved information on composition (using energy-dispersive X-ray spectroscopy or EDS) and local bonding and coordination (through EELS), makes STEM-EELS a powerful tool for determining oxidation state in materials at the sub-nanometer scale. An open question is the extent to which Fe^{3+} and Fe^{2+} are distributed randomly or locally within a glass structure, and STEM-EELS has the capability of addressing this.

The high brightness and focused probe of the aberration-corrected STEM enable fast acquisition of data and low detection limits in EELS. However, the highly focused beam can cause significant damage to sensitive samples, including loss of material or breaking of bonds, which can change valence or coordination states of atoms (Egerton, 2011). Glasses and other amorphous silicates are known to be highly susceptible to damage caused by the electron beam during microscopy measurements. Mechanisms of both oxidation (Garvie et al., 2004; Lauterbach et al., 2000; Van Aken et al., 1998) and reduction (McCartney et al., 1991; Smith et al., 1987) due to effects of the electron beam have been measured in transition metal-bearing materials. Jiang and co-workers (Jiang and Spence, 2010; Jiang, 2013) have shown that the induced electric field created by the uncompensated emission of secondary and Auger electrons in insulating materials (Cazaux, 1995) drives diffusion of cations from an area much larger than the probe. Diffusion of network-modifying cations (mono- and divalent species) in silicate glasses is relatively fast compared to what is observed in many crystalline materials, and it is more easily charge compensated, with no crystal-chemical constraints to overcome (Zhang et al., 2010). Thus the effects of beam damage on glass structure, composition, and oxidation state are

important consequences of measurement. This paper seeks to shed light on these issues, while also informing the question of long vs. short-range ordering of Fe^{3+} and Fe^{2+} in glasses.

Methods

Homogenous, synthetic glasses of basaltic, andesitic and rhyolitic composition were prepared for EELS measurements. Synthetic glass starting compositions were generated for a wide range of geologically-relevant compositions. The iron contents of the samples range from 1.7-3.7 wt% FeO in rhyolitic to 7-12 wt% FeO in andesitc and basaltic compositions (Table 1).

Syntheses

Starting compositions were produced by weighing out appropriate amounts of Alfa Aesar Puratronic oxide and carbonate powders, and then grinding the mixtures by hand in an agate mortar under ethanol for one hour, followed by decarbonating (if carbonates are present) at 800°C for 2 hours. Oxide mixes were used directly in the experiments without a glassing step. A mixture of sample powder (~100 mg) and polyvinyl alcohol was used to adhere the sample to the wire loop.

Equilibration experiments were run in a vertical 1-atm gas mixing furnace at Tufts University using the Pt (or Re) wire-loop technique (Presnall and Brenner, 1974). Re loops were used for low f_{O2} runs (f_{O2} < QFM [quartz-fayalite-magnetite]). Fe solubility in the Re is low under the conditions of these experiments (Borisov and Jones, 1999). Pt-loops were pre-doped using powders of the identical starting composition for 6 hours at T_{max} and the f_{O2} intended for the experiment. Glassy material was dissolved off the Pt-loop using a 50:50 mixture of heated HF and HNO_3 and the loop was then used for an experiment. These procedures were followed to reduce but, generally, not eliminate Fe losses to the wire during an experiment.

The f_{O2} was measured using an $SIRO_2$ yttria-doped zirconia oxygen sensor located adjacent to the sample and temperatures were measured using a type S thermocouple. Oxygen fugacities were fixed either by flowing air or an H_2-CO_2 gas mixture corresponding to the QFM or IW (iron-wüstite) buffer for the maximum temperature of an experiment. The gas composition was held constant during cooling. For H_2-CO_2 gas mixtures, the gas becomes more reducing than QFM during cooling because T-log f_{O2} relationships for the constant composition H_2-CO_2 gas and the QFM buffer are different. Based on the Deines et al. (1974) tables, this effect should be no greater than 0.23 log units for our experiments. Each glass composition was run under all three f_{O2} conditions, producing a range of Fe^{3+} concentrations in the melt for use in calibration.

All experiments were initiated by inserting the sample into the hot spot under the desired gas mixture at ~1000°C, followed by ramping to the composition-dependent peak temperature at 500°C/hr. These glass equilibration experiments remained at this peak temperature for the duration of the run necessary to ensure melt homogenization, usually 1- 24 hours. Samples were then drop-quenched into deionized water. Using the calculations of Birnie and Dyar (1986) for quenching into water from 1400°C, this would result in an average quench rate of ~247°C/s. Recovered run products were prepared for Mössbauer and EELS analyses. Mössbauer mounts were prepared using the entire volume of one-half of one bead, whereas EELS fragments were extracted by gently crushing the other half-bead and removing a few of the resultant grains. Thus the portion of the sample used for the EELS analysis may not reflect the average cooling rate as its precise location within the bead was unknown.

Independent Quantification of Fe^{3+}

Mössbauer spectra of the samples were acquired with a WEB Research Co. constant acceleration MB spectrometer equipped with a Janis Research Co. model 850 closed-cycle He

refrigerator at Mount Holyoke College. A ~50-100 mCi^{57}Co in Pd source and 24-hour acquisition times were used, and the data were referenced to the midpoint of an α-Fe foil spectrum (6 μm thickness and 99% purity). Roughly half of the material from each glass bead was lightly ground under acetone with sugar to reduce particle size, reduce the angularity of particles by coating them with sucrose, and distribute the absorber evenly over the sample holder to optimize signal to noise; the powder mixture was mounted in a sample holder confined by cellophane tape. The resultant sample thickness was less than 1 mg Fe/cm^2, below the thin absorber thickness approximation of Long et al. (1983).

Mössbauer data were modeled using an in-house program from the University of Ghent, in Belgium called DIST_3E, which uses model-independent quadrupole splitting distributions for which the subspectra are constituted by Lorentzian shaped lines. This program does not presume any particular shape of the distribution. Fe^{3+} and Fe^{2+} doublet areas were discriminated on the basis of their hyperfine parameters (Dyar et al., 2006). In the absence of data on recoil-free fractions for Fe in glasses, peak areas were assumed to correspond directly to the abundance of the species in the samples (Dingwell, 1991; Mysen et al., 1985). It is recognized that this assumption may unavoidably contribute to the errors on the Fe^{3+} and Fe^{2+} distributions in this sample. Thus, the errors on %Fe^{3+} from Mössbauer are estimated to be roughly ±1–3% (Dyar, Melinda Darby, 1984). The Mössbauer results are used to compare with the redox ratios determined by EELS.

The samples in the entire suite were also analyzed by x-ray absorption spectroscopy as reported in Dyar et al. (2016b). In that study, a focused synchrotron beam of 1-10 μm^2 was used with samples ~30 μm thick, and the Fe^{3+} contents were found to be strikingly homogeneous within each glass. The electron microprobe results of studies of these beads show standard

deviations (Table 1) that also indicate homogeneity at the scale of the electron microprobe (<1 μm). Thus, the previous work establishes that the Fe redox state in the samples in the present study is homogeneous at scales of 1-10 μm, an area roughly three orders of magnitude larger than the EELS technique used here.

STEM Measurements

Small pieces of each sample were embedded in epoxy and microtomed, then placed on Quantifoil carbon support film TEM grids. The samples vary in thickness due to chattering of the microtome blade; measurements were constrained to regions where the thickness t was less than the electron mean free path λ (e.g., $t/\lambda < 1$). Samples are stored under nitrogen and baked under vacuum at 140°C for 8 hours to drive off adsorbed water before analysis in the microscope. One sample was baked and analyzed on several different occasions, but no systematic differences were seen when comparing data collected on different days.

EELS and EDS data were collected on PRISM, the NION UltraSTEM200 at the U.S. Naval Research Laboratory, equipped with a Gatan Enfinium ER EEL spectrometer and a windowless, 0.7 sr Bruker SSD-EDS detector. Measurements were done at a 60 kV and 200 kV and 12-150 pA with an electron probe size of 0.1-0.2 nm. Due to beam broadening effects, the diameter of the cone containing 90% of emerging electrons at 200 kV is ~1.5 nm for a sample ~50 nm thick (Williams and Carter, 1996); the diameter of the cone depends on the sample thickness and most of the intensity is focused within a narrower volume. Spectra were collected as spectrum images (SI), with a spectrum collected for each spatial pixel to map possible variations in thickness, composition, and oxidation state. SIs were generally ~5×10^3-10^4 nm^2, limited by the need to use only relatively thin regions of the glass. Pixel sizes varied depending on the size of the SI and chosen pixel density; in some cases the pixel size was smaller than the

beam interaction diameter, affecting the total dose to each pixel. In order to keep doses low while still acquiring some signal, the beam is stationary in each pixel for a set period of time (0.01-0.5s), and thus individual spectra are quite noisy and must be summed over several pixels. The energy dispersion is 0.05-0.1 eV/channel, and SIs were collected separately for Fe L-edges and zero-loss peaks (ZLP). Energy resolution, measured from the ZLP, is 0.4-0.45 eV. In many regions, O K-edge measurements were also obtained. EDS data were also acquired as spectral maps; the beam was scanned at a rate of 16 µs/pixel for 230-500 frames. Quantification was done using the Cliff-Lorimer method with default *k*-factors; samples were thin enough to not require absorption correction.

Peak alignment to compensate for energy drift during SI acquisition was carried out using Gatan Digital Micrograph software to first align the zero-loss peak then apply the same shift at each pixel in the related core-loss SI. This does not correct energy shifts that affect the entire SI equally, but fitting methods described later were used to account for small shifts.

Quantification of EELS Results

Iron L-edges in EEL spectra are caused by the excitation of inner shell (2*p*) electrons to the unoccupied 3*d* orbitals. There are two distinct edges or "white lines", L_3 and L_2. EEL spectra of Fe^{2+}- and Fe^{3+}- bearing minerals show distinct edge shapes and chemical shifts that depend on the oxidation state and the symmetry and coordination of the atom site. Excitations from both Fe^{2+} and Fe^{3+} contribute to the shapes and intensities of L_3 and L_2 but at slightly different energies. Published methods for quantifying EELS-based $Fe^{3+}/\Sigma Fe$ include variations of three basic methods: ratios of the integral in two different energy regions (e.g., Cavé et al., 2006; Schmid and Mader, 2006; Tan et al., 2012; Van Aken et al., 1998; Van Aken and Liebscher, 2002); ratios of intensity or integral of Gaussian, Lorentzian or Voight peaks fitted to the L_3 peak

(e.g., Calvert et al., 2005; Van Aken and Liebscher, 2002); and linear least-squares fitting of two or more end-member spectra to the unknown (e.g., Deboudt et al., 2012; Garvie and Buseck, 1998; Thompson et al., 2016). Several workers have noted that white-line window ratios are not applicable for samples with <10 at% Fe, below which the L_2 peak becomes small relative to the noise (Calvert et al., 2005; Cavé et al., 2006), whereas end-member mixing requires >~6 at% Fe (Calvert et al., 2005).

Our samples have Fe < 5 at% (FeO < 10.5 mol%), which means the peak fitting method is the most accurate (Calvert et al., 2005). The Gaussian fit method (GM) quantification requires isolation of the white lines from the background (Calvert et al., 2005; Van Aken et al., 1998). Spectra are summed over regions of interest within spectrum images to increase signal-to-noise, and only regions with relative thickness $t/\lambda < 0.9$, where t is the absolute thickness of the sample and λ is the mean free path (~130 nm in basaltic glass at 200 kV (Egerton, 2011)), are used in order to reduce multiple-scattering effects. The background intensity is removed using a power-law fit to the pre-edge region extrapolated over the full energy range, then a multiple arctangent background is fit following Calvert et al. (2005), such that the inflection point is aligned with each peak maximum in an iterative process. Three peaks are then fitted to the L_3 white line, constraining them to center at 707.8±1 eV (P1), attributed primarily to Fe^{2+}, 709.5±1 eV (P2) for Fe^{3+}, and a high-energy shoulder at 712±1.5 eV not attributed to a specific valence state (Calvert et al., 2005; Van Aken and Liebscher, 2002). Many Fe^{3+}-bearing minerals with octahedral coordination also have a peak at ~707.8 eV (Garvie and Buseck, 1998); Fe^{3+} in tetrahedral coordination has a single peak at slightly lower energy than the octahedral Fe^{3+} when seen in the same crystal (Haruta et al., 2011). However, the possible energy shift due to coordination could also be affected by distortion of the tetrahedra and octahedra, so we use only a single peak to fit

the Fe^{3+} component and allow the peak center energy to vary slightly. To account for possible energy drift during scanning and acquisition, peak energy is allowed to vary slightly from published values, but P1 and P2 are constrained to be no more than 2.2 eV apart. Fig. 1 shows fits to a number of standard and glass spectra. We calculate the integral intensity of the peak centered at 709.5 eV (P2) relative to the summed integral intensity of P1 and P2, $I_{P2}/(I_{P1}+I_{P2})$, to give us a relative measure of oxidation state (Rox). Higher-energy peaks are also fit but not included in the quantification; including peak 3 (cyan in Fig. 1) in the ratio calculation alters the precise value but does not significantly change the Rox of individual samples relative to each other. Using similar approaches, Van Aken and Liebscher (2002) and Calvert et al. (2005) find a linear relationship between this value and $Fe^{3+}/\Sigma Fe$ with no orientation effects. Errors for the Rox are determined from the residual of the fitted curves.

Results

A number of sample Fe L-edge spectra are presented in Fig. 1. Spectra from San Carlos olivine ($^{[6]}Fe^{2+}$) and hematite ($^{[6]}Fe^{3+}$) are also shown for comparison. The experimental spectra in Fig. 1 were all collected from IW-basalt3 during the same session. The spectra in Fig. 1 show a large range of intensity variations for the ~708 eV and ~709.5 eV peaks, indicating they cover almost the full range of possible oxidation states. Additionally, although hematite and silicate minerals with $^{[6]}Fe^{3+}$ have a small peak near 708 eV, this shoulder is much smaller in the oxidized glass indicating structural differences rather than valence state differences and leading to Rox higher than that calculated for hematite. Rox values calculated from the GM fit compared with Mössbauer data are shown in Fig. 2. Glass equilibrated at IW is expected to have $Fe^{3+}/\Sigma Fe$ ~0.1 based on Mössbauer measurements, and glass equilibrated in air has $Fe^{3+}/\Sigma Fe$ = 0.9-1.0. The Mössbauer data is consistent with $^{[6]}Fe^{3+}$ and $^{[4]}Fe^{3+}$ being present in all glasses; there does

not appear to be a systematic difference in $^{[6]}Fe^{3+}/^{[4]}Fe^{3+}$ in oxidized versus reduced glasses. The reduced samples measured using EELS, including two IW-basalts, four QFM-basalts, and one IW-andesite, show a large range in Fe oxidation states based on the EELS data. Samples equilibrated in air and CO_2 are oxidized, with much less variation in relative peak intensities.

Rhyolite samples are very low in Fe (<1% of total ions), and spectra can be quite noisy. In measurements with signal-to-noise (SNR) above ~3, Fe appears quite oxidized; lower SNR is not trusted to provide robust results. The dose and dose rate are both quite high compared to what was used in measurements of basalt and andesite samples, and the large error bars on Rox prevent strong conclusions about the oxidation state or the intra-sample variability. Rhyolite samples are not considered further.

Beam damage is known to cause oxidation in silicates (Garvie et al., 2004). While data at moderately high doses and dose rates are on average more oxidized than the full dataset for a reduced sample (Fig. 3), both oxidized and reduced regions are present in the lower-dose measurements (Fig. 3a inset). Where measurements were repeated on the same sample region, the repeat measurements were often more oxidized than the initial measurement. Fig. 4 shows how Rox changes as dose (D) increases; most of the data plot above zero, indicating an increase in oxidation. However, neither dose nor dose rate is consistently related to the change in oxidation state between different regions of the same sample, and a simple relationship cannot be determined. Only a few spectra were acquired at very high doses because damage becomes apparent in images at these conditions. Fig. 5 shows a high-angle annular dark field (HAADF) image of QFM-basalt6 after acquisition of an EELS SI. HAADF images are sensitive to the density and composition of the material, and the rectangular mottled region where the SI was

acquired shows local variation induced by the beam. The three spots in the upper right of the image are also beam damage.

A stationary electron beam on the silicate glass samples dwelling for several seconds (never used for the oxidation state measurements) leads to the creation of dark "spots" (or lines where the sample has drifted) ~10 nm across in HAADF (z-contrast) images (Fig. 6a). EDS measurements of glass with no visible damage compare well with the nominal glass composition, although some Na and possibly Mg has been lost (Table 2, Fig. 6b). However, where the beam has dwelled for several seconds, the sample is highly depleted in all cations other than Si. The bright rim surrounding the dark spots is slightly enriched in Al and Ca relative to the undamaged glass. In low-loss EELS measurements, the main plasmon peak, ~22 eV, associated with Si-O, is slightly broader inside the dark spot, and small shoulders at ~35 eV and 55eV (Fe) are no longer visible (Fig. 6c).

There is no overall relationship between thickness and Rox in any of the samples (Fig. 7a). Data filtered to show only samples with small thickness variations and low doses show a smaller range in oxidation states than the full dataset, but at the scales of these measurements, there is still both significant variation in the QFM- and IW-buffered samples and no trend pointing to a specific experimental cause of the variation, indicating it is likely inherent to the sample.

Within individual SIs, there is evidence of oxidation state variation on the scale of 10s of nanometers and of crystalline or nano-crystalline regions in the glass that have different oxidation state from their surroundings. Fig. 8a shows two regions in QFM-basalt6 within 50 nm of each other with visible lattice fringes and different oxidation states, as demonstrated by the EEL spectra in Fig. 8b. Magnetite grains 50-100 nm across have also been identified (Fig. 8c and

d), although magnetite is not detected in Mossbauer measurements (detection limit ~0.5%) or the electron microprobe measurements using a 500-1000 nm beam.

Discussion

Quantification of EELS data relies on relationships with standards, whether to create curves relating window or peak intensity ratios to $Fe^{3+}/\Sigma Fe$ or to fit end-member spectra. The high values of Rox = $I_{P2}/(I_{P1}+I_{P2})$ measured here in the oxidized glasses, higher than that in hematite following the same fitting procedure, indicate that a significant portion of the Fe^{3+} measured in those samples is in tetrahedral coordination. Silicate crystals such as $^{[6]}Fe^{3+}$-bearing garnet have smaller ~708 eV peaks than oxides such as hematite, while the low energy L_3 peak virtually disappears in minerals with $^{[4]}Fe^{3+}$ (Calvert et al., 2005; Garvie et al., 1994; Van Aken and Liebscher, 2002). A 0.5 eV shift between $^{[4]}Fe^{3+}$ and $^{[6]}Fe^{3+}$ has been shown in brownmillerite ($CaFeO_{2.5}$) (Haruta et al., 2011), but such a shift, if it occurs in silicate glasses, is not observable consistently in our data. The multiple coordination sites available to Fe in glasses, including $^{[5]}Fe$ (Farges et al., 2004), also complicate quantification of the oxidation state. However, even given the relatively high error in Rox due to structural complexities and low Fe content, the EELS and EDS measurements contribute to our understanding of silicate glass structure, beam sensitivity, and alteration during sample preparation.

Sample Damage

It is clear that exposure to the beam leads to significant changes in both Fe oxidation state and overall composition within short periods of time, and in many cases, reduced samples become oxidized with increasing dose. For repeat measurements made sequentially in the same location, there is often a relationship between dose and increasing oxidation state (Fig. 4). The slope of the trend is not consistent, but the many contributing factors (e.g., initial oxidation state,

thickness, dose rate, intermediate-range structure) are difficult to separate. However, it is also the case that the most reduced spectra for each sample do not come from either the thickest regions or the lowest-dose measurements. For most samples, filtering out data from the highest doses does not significantly decrease the spread in oxidation states, and even then, reduced samples are still measured at relatively high doses (see IW-andesite4 in Fig. 3). At the highest doses used in this study, there is the suggestion that oxidation state of the samples becomes more reduced again. In Fig. 4, multiple points of the same glass plot at exactly the same thickness, which indicates more than two SIs were repeated in the same region; in several cases, these plot both above and below zero, indicating Rox first increases then decreases with subsequent measurements.

Jiang (2013) has shown that damage due to the electric field created by the beam and secondary electron emission should be independent of sample thickness. The size of the spot created by a stationary beam and the diffusion of cations away from this spot, as indicated by the EDS measurements, is consistent with this type of damage. Activation energy for diffusion in silicate glasses follows the order Ca ~ Mg ~ Fe^{2+} < Fe^{3+} < Al < Si ~ O (Zhang et al., 2010). Although Al and Fe^{3+} are network formers in the glass and therefore somewhat less mobile than network modifying cations (i.e., Mg, Ca, Fe^{2+}), the energy of the electron beam is clearly enough to drive diffusion of these components also.

During repeated measurements, there is no change in t/λ, which indicates that material is not being lost due to sputtering knock-on damage. Relative t/λ does change for the highly altered regions in the dark beam spots (Fig. 6), but this change is related to the difference in density of amorphous silica versus that of basaltic or andesitic glasses (~2.8 g/cc for basaltic glass at room temperature versus ~2.2 g/cc for fused silica), which changes the mean free path λ of the

material. Although the signal-to-noise ratio for the Fe L-edge becomes too low to determine the oxidation state in the highly damaged regions because of the loss of Fe, the low-loss spectrum (Fig. 6c) does show changes from loss of Fe, and a small change in the main peak related to Si-O bonding. Similar localized damage related to the beam spot is apparent in measurements done at 60 kV as well as 200 kV.

Electron beam damage can occur by several different mechanisms, including both elastic and inelastic interactions between the electrons and the material. Inelastic interactions, such as radiolysis and electrostatic charging, generally have threshold energies much lower than those used in TEM, and dose or dose rate thresholds instead determine the degree of damage in a material (Jiang and Spence, 2012). Elastic interactions become important at higher beam energies, where the incident electron energy is high enough that collision with a nucleus causes displacement within the lattice (knock-on damage) or sputtering from the surface. Bulk displacement via this mechanism has the largest effect on light elements; the knock-on threshold for oxygen in silicates is below 200 keV. However, the similarity in beam damage features when samples are viewed using both 60 kV and 200 kV indicates that no advantage is gained by using the lower accelerating voltage for silicate glasses. Rather, at higher accelerating voltage, thicker specimens can be used for spectroscopy due to the longer mean free path of the higher energy electrons (Egerton, 2011), and the dose can therefore possibly be spread through a slightly larger volume of material.

For the lower dose oxidation state measurements (Fig. 3a inset region), the electron beam does not dwell long enough to create visible damage in the glass. However, the semiconducting nature of basaltic glass (Jurado-Egea et al., 1987) promotes electron-hopping between neighboring Fe^{3+} and Fe^{2+}, as well as less localized charge transport away from the beam. Thus,

changes in the electronic structure of the glass could be very rapid and contribute to the apparent oxidation state of the glass (Weigel et al., 2008). Thermally activated electron localization has been observed in crystalline silicates with mixed-valence Fe (Fei et al., 1994), indicating beam heating may play a role here, as well as in facilitating cation diffusion. Limited cation motion may take place, even given low doses and short dwell times, which could lead to increased oxidation state. The electric field created by the net emission of secondary electrons and ionization of the glass causes cations to diffuse away from a dwelling beam, increasing the oxygen/cation ration and "oxidizing" the sample. The small beam and relatively high mobility of cations in glasses means that only a very short time would be required for cations to move a very short distance out of the volume measured by the beam. Based on glass density and composition, ~100 Fe ions are expected within the beam interaction cone in a 50 nm thick wedge, and diffusion of just a few ions could alter the local $Fe^{3+}/\Sigma Fe$. Additionally, Fe^{2+} is going to be much more mobile than Fe^{3+} because of its position in the glass as a network modifier, whereas Fe^{3+} is often a network former.

We searched for a relationship between the slope of the change in oxidation state with dose and either the thickness or dose rate, as well as total dose (Fig. 4). While the slope of the change is similar for many samples, the variation in slope is not related to any obvious property. The local thermal conductivity is unknown, and heating could play a role in the rate of damage. All measurements were done on glass suspended over a hole, but distance from the amorphous carbon substrate and the size of the glass shard could lead to undetermined variations. Where more than two measurements were done sequentially on the same region, the rate of change between the second and third measurements is almost always less than between the first and

second, which could be due to the change in concentration in the region or structural changes decreasing the diffusivity.

Surface Oxidation

Oxidation by the electron beam affects both thick and thin areas of the sample. However, in several locations, thin regions are more oxidized than the spatially closely related relatively thick regions, independent of actual thickness. Both thick and thin regions of the same SI show similar changes in oxidation state upon subsequent measurements. This indicates that some surface oxidation takes place during sample preparation and insertion in the microscope; a thin uniform layer of glass that is highly oxidized relative to the bulk glass in that region would have a larger relative effect on thin regions compared to thicker regions where the oxidized layer is a smaller percentage of the total. Oxidized coatings on metals several nanometers thick are known to form in seconds to minutes of exposure to ambient air (Suzuki et al., 1997), but the thickness of such layers are highly material dependent.

Surface oxidation effects are not uniform, however. For 20 different SI that were noted to have thickness variations over 20%, four show no change in oxidation state with thickness above the error of the GM fit, two have thin regions that are actually more reduced than the thick regions, and the remaining 14 measurements have a range of slopes for the change in oxidation state with the relative change in thickness, $(Rox_1\text{-}Rox_2)/(t_1\text{-}t_2)$ where $t_1 > t_2$ (Fig. 9a). The change in oxidation state per thickness change indicates that the oxidized surface layer of the glass varies with the initial oxidation state of the glass, if we assume that the altered film is uniformly oxidized (Fig. 9b). Using the thickness of the oxidized film on the glasses calculated to initially be fully reduced (~20 nm, assuming mean free path $\lambda \sim 130$ nm for silicate glass(Egerton, 2011)), and assuming the samples were exposed to oxidizing conditions for 100 s, from the

approximation $D = x^2/t$, we find $D \sim 10^{-18}$ m^2/s, which is consistent with polaron mobility based on extrapolation of basaltic glass electrical conductivity measurements to room temperature (Presnall et al., 1972).Variation in both altered layer thickness and unaltered oxidation state is seen in calculations for regions in the same sample. In glasses that are initially more oxidized, there is much smaller driving force for the formation of such a film, as evidenced by the thinner oxidized film. The samples were stored in dry N_2, baked overnight under vacuum, measured usually within several days of microtoming. The rate of H_2O diffusion in silica at the bake temperature is fast enough to affect up to 10s of nanometers of material at high vapor pressure (Doremus, 1995). However, our samples are baked at very low vapor pressure, and diffusion at room temperature, where again, vapor pressure of water around the samples was kept very low, is several orders of magnitude slower. Thus the notable effect of surface oxidation in these samples indicates that possible alteration effects cannot be disregarded even in very carefully prepared samples. The rate of oxidation with damage due to the electron beam is consistent between thick and thin regions, again supporting diffusion away from the beam as the main mechanism by which beam damage occurs.

Sample Heterogeneity

The glass samples are inhomogeneous at the nanometer scales applicable to TEM measurements. This variability cannot be accounted for solely by beam damage and surface oxidation; the calculated initial Rox, which should account for any oxidized surface layer, exhibits almost the full range shown in Fig. 9b when filtered to show only low doses. Additionally, nano-crystalline regions are identified in the samples, including grains of magnetite that are present at concentrations too low to be detected using Mössbauer spectroscopy. Incomplete equilibration of the samples during synthesis could lead to these signals, as well as

nucleation during quench. Other micro-analytical techniques have shown that the suitability of many standard materials depends on the scale of measurements being done and that materials that are homogenous optically or at low resolution in the microprobe may have spatially-varying compositions when measured using SIMS, for example. The EMPA, XANES, and Mössbauer measurements completed on these glasses (Dyar et al., 2016b) were done using orders of magnitude larger volumes of material (Table 3). Measurements of oxidation state at the micrometer scale suggest that the redox ratio is constant throughout a millimeter-sized basaltic glass sample, even when the sample is not fully equilibrated with the environment (Roskosz et al., 2008). It is possible that while electron transfer in Fe-bearing silicate glasses is fast enough to be fully homogenized, the interaction of the electron beam with the non-random structure of the glass causes fine-scale EELS measurements to reflect the effect of the glass structure on the stabilization of certain electronic configurations rather than the initial or bulk oxidation state. Thus even though some damage is occurring very rapidly in the sample, the data are useful in interrogating the initial variability in the glass.

In addition to having complicated oxygen coordination, with both Fe^{2+} and Fe^{3+} possible in four-, five- and six-fold coordination (e.g., Mysen and Richet, 2005; Weigel et al., 2008), clustering of at least two and possibly more Fe ions in known to occur in a number of glasses with Fe_2O_3 > 1 mol% (Bingham et al., 1999; Rüssel, 1993; Weigel et al., 2008). Some evidence indicates iron-rich structural units within the silicate glass may resemble magnetite (Virgo and Mysen, 1985), although other work suggests clusters of $^{[5]}Fe$ are present in iron-bearing alkali-silicate glasses (Weigel et al., 2008). The presence of nano-crystalline magnetite in the glass here, and its ease of nucleation in basalt glasses (Beall and Rittler, 1976) support the segregation of Fe in some regions. Alkalis and alkaline-earths have different effects on the presence,

stabilization, and clustering of Fe^{3+} in tetrahedral coordination depending on cation size and concentration ratio when several cations are present (Bingham et al., 2002, 2007; Vercamer et al., 2015). Such clusters could exacerbate beam effects in certain regions of the glass relative to others and could explain the spread in oxidation states even in air- and CO_2-equilibrated samples that would not otherwise be expected to have significant Fe^{2+}. Fe^{3+}/Fe^{2+} is known to vary in alkali-silicate glasses with composition even when prepared under the same conditions (Mysen et al., 1980).

Molecular dynamics simulations examining dynamic heterogeneities in amorphous calcium aluminosilicates find regions of ~100 atoms with higher or lower concentrations of Ca and Al relative to Si (Vargheese et al., 2010). Network modifying cations in aluminosilicate glasses have been shown to bond preferentially with SiO_4-tetrahedra as opposed to AlO_4-tetrahedra, but the strength of the preference depends strongly on the cation field strength (Lee et al., 2005). Similarly, Fe^{2+} and Fe^{3+} may exhibit preference in a melt (or glass) and become segregated. Measurements of relaxation times in ternary silicate glasses have also found two distinct structural domains (Zhang et al., 2013). The short- and intermediate-range ordering in the glass and difference in both coordination and mobility between Fe^{2+} and Fe^{3+} mean that variations in oxidation state measured over the scale of 10s of cubic nanometers are consistent with previous data and ideas of glass structure. The total amount of material measured in all analyses presented here, much less any single sample, while including many individual measurements, is smaller than the volume encompassed by a single microprobe measurement at 5 kV, which is ~0.5 μm^3. The volumes sampled by other techniques that do not see heterogeneity in the glass are also considerably larger than that in STEM (Table 3).

Glass preparation techniques such as pulsed laser deposition and chemical vapor deposition (CVD) are known to produce amorphous thin films with very different structure from melt-quenched glasses due to the much faster quench rate and differences in precursor structure. These differences are reflected in the glasses having less short- and medium-range structural and compositional ordering than glass quenched from a melt (i.e., more "defects") (Lee and Ahn, 2014). Such glasses may be more fitting for use as standards in nano-scale measurement techniques, although direct links to other measurements techniques would be difficult due to the sample sizes. They would be poor representations of the structure of terrestrial magmatic glasses, but they could serve as analogs for amorphous materials condensed in interstellar medium or during solar system formation (Speck et al., 2011).

Implications

EELS and EDS in ac-STEM are powerful techniques for measuring volumes of material inaccessible to other measurements. Synthetic basaltic, andesitic, and rhyolitic glasses, which are often used as analogs for natural materials and calibration standards for many techniques, show nano-scale compositional and structural heterogeneities not detected using other techniques. This heterogeneity is evidence of nucleation and crystallization processes that can often only be inferred from bulk measurements. Careful measurements of analog materials at the same scales as those done in natural materials provide necessary context for expectations of variability and rates of nucleation or alteration. In many geological contexts, length-scales can be a proxy for time-scales and observations at the nano-scale allow for study of processes occurring over very short periods of time during quench or condensation. Nano-scale oxidation measurements in planetary materials, for instance, have the potential to provide constraints on environments during solar system formation. However, it is important to note that ac-STEM analyses may not

provide reliable measurements of "bulk" silicate glass composition or oxidation state if thin sample regions are too small, which makes direct linkage to other measurements and properties challenging. Alternative sample preparation techniques that produce large areas of uniform thickness, such as use of focused ion beam (FIB) microscopy, could provide a way to avoid this limitation. Our results show that amorphous material can be quickly damaged and oxidized by the electron beam, but changes in material composition induced by the electron beam can be used to make inferences about structure and diffusion in glasses.

Acknowledgements

This work was supported by the RIS^{4}E node of NASA's Solar System Exploration Research Virtual Institute. It is SSERVI publication number SSERVI-2016-031. We thank A. Brearly, F. Langenhorst, and B. Mysen for thorough and constructive reviews.

References

Bajt, S., S. Sutton, and J. Delaney (1994) X-ray microprobe analysis of iron oxidation states in silicates and oxides using X-ray absorption near edge structure (XANES). Geochimica et Cosmochimica Acta, 58, 5209-5214, doi: 10.1016/0016-7037(94)90305-0.

Bancroft, G.M., A.G. Maddock, and R.G. Burns (1967) Applications of the Mössbauer effect to silicate mineralogy—I. Iron silicates of known crystal structure. Geochimica et Cosmochimica Acta, 31, 2219-2246, doi: 10.1016/0016-7037(67)90062-2.

Beall, G.H., and H.L. Rittler (1976) Basalt glass ceramics. The American Ceramic Society Bulletin, 35, 579-582.

Bingham, P.A., J.M. Parker, T. Searle, J.M. Williams, and K. Fyles (1999) Redox and clustering of iron in silicate glasses. Journal of Non-Crystalline Solids, 253, 203-209, doi: 10.1016/S0022-3093(99)00361-0.

Bingham, P.A., J.M. Parker, T.M. Searle, J.M. Williams, and I. Smith (2002) Novel structural behaviour of iron in alkali–alkaline-earth–silica glasses. Comptes Rendus Chimie, 5, 787-796, doi: 10.1016/S1631-0748(02)01444-3.

Bingham, P.A., J.M. Parker, T.M. Searle, and I. Smith (2007) Local structure and medium range ordering of tetrahedrally coordinated Fe^{3+} ions in alkali–alkaline earth–silica glasses. Journal of Non-Crystalline Solids, 353, 2479-2494, doi: 10.1016/j.jnoncrysol.2007.03.017.

Birnie, D.P., and M.D. Dyar (1986) Cooling rate calculations for silicate glasses. Journal of Geophysical Research, 91, 509-513, doi: 10.1029/JB091iB04p0D509.

Borisov, A., and J.H. Jones (1999) An evaluation of Re, as an alternative to Pt, for the 1 bar loop technique: An experimental study at 1400° C. American Mineralogist, 84, 1528-1534, doi: 10.2138/am-1999-1006.

Bourdelle, F., K. Benzerara, O. Beyssac, J. Cosmidis, D. Neuville, G. Brown, Jr., and E. Paineau (2013a) Quantification of the ferric/ferrous iron ratio in silicates by scanning transmission X-ray microscopy at the Fe $L_{2,3}$ edges. Contributions to Mineralogy and Petrology, 166, 423-434, doi: 10.1007/s00410-013-0883-4.

Bourdelle, F., T. Parra, O. Beyssac, C. Chopin, and O. Vidal (2013b) Clay minerals as geo-thermometer: A comparative study based on high spatial resolution analyses of illite and chlorite in Gulf Coast sandstones (Texas, U.S.A.). American Mineralogist, 98, 914-926, doi: 10.2138/am.2013.4238.

Calvert, C.C., A. Brown, and R. Brydson (2005) Determination of the local chemistry of iron in inorganic and organic materials. Journal of Electron Spectroscopy and Related Phenomena, 143, 173-187, doi: 10.1016/j.elspec.2004.03.012.

Cavé, L., T. Al, D. Loomer, S. Cogswell, and L. Weaver (2006) A STEM/EELS method for mapping iron valence ratios in oxide minerals. Micron, 37, 301-309, doi: 10.1016/j.micron.2005.10.006.

Cazaux, J. (1995) Correlations between ionization radiation damage and charging effects in transmission electron microscopy. Ultramicroscopy, 60, 411-425, doi: 10.1016/0304-3991(95)00077-1.

Christie, D.M., I.S.E. Carmichael, and C.H. Langmuir (1986) Oxidation states of mid-ocean ridge basalt glasses. Earth and Planetary Science Letters, 79, 397-411, doi: 10.1016/0012-821X(86)90195-0.

Cottrell, E., and K.A. Kelley (2011) The oxidation state of Fe in MORB glasses and the oxygen fugacity of the upper mantle. Earth and Planetary Science Letters, 305, 270-282, doi: 10.1016/j.epsl.2011.03.014.

Deboudt, K., A. Gloter, A. Mussi, and P. Flament (2012) Red-ox speciation and mixing state of iron in individual African dust particles. Journal of Geophysical Research: Atmospheres, 117, doi: 10.1029/2011JD017298.

Deines, P., R.H. Nafziger, G.C. Ulmer, and E. Woermann (1974) Temperature-oxygen fugacity tables for selected gas mixtures in the system C-H-O at one atmosphere total pressure, 129 pp., College of Earth and Mineral Sciences, Pennsylvania State University.

Deubener, J. (2005) Structural aspects of volume nucleation in silicate glasses. Journal of Non-Crystalline Solids, 351, 1500-1511, doi: 10.1016/j.jnoncrysol.2004.04.028.

Dingwell, D.B. (1991) Redox viscometry of some Fe-bearing silicate melts. American Mineralogist, 76, 1560-1562.

Doremus, R.H. (1995) Diffusion of water in silica glass. Journal of Materials Research, 10, 2379-2389, doi: 10.1557/JMR.1995.2379.

Dyar, M.D. (1984) Precision and interlaboratory reproducibility of measurements of the Moessbauer effect in minerals. American Mineralogist, 69, 1127-1144.

Dyar, M.D. (1984) Experimental methods for quenching structures in lunar-analog silicate melts: Variations as a function of quench media and composition. Journal of Geophysical Research, 89, C233-C239, doi: 10.1029/JB089iS01p0C233.

Dyar, M.D., and D.P. Birnie (1984) Quench media effects on iron partitioning and ordering in a lunar glass. Journal of Non-Crystalline Solids, 67, 397-412, doi: 10.1016/0022-3093(84)90165-0.

Dyar, M.D., J.S. Delaney, S.R. Sutton, and M. Schaefer (1998) Fe^{3+} distribution in oxidized olivine: A synchrotron micro-XANES study. American Mineralogist, 83, 1361-1361, doi: 10.2138/am-1998-1227.

Dyar, M.D., E.W. Lowe, C.V. Guidotti, and J.S. Delaney (2002) Fe^{3+} and Fe^{2+} partitioning among silicates in metapelites: A synchrotron micro-XANES study. American Mineralogist, 87, 514-522, doi: 10.2138/am-2002-0414.

Dyar, M.D., D.G. Agresti, M.W. Schaefer, C.A. Grant, and E.C. Sklute (2006) Mössbauer spectroscopy of earth and planetary materials. Annual Review of Earth and Planetary Sciences, 34, 83-125, doi: 10.1146/annurev.earth.34.031405.125049.

Dyar, M.D., E.A. Breves, M.E. Gunter, A. Lanzirotti, J.M. Tucker, C.J. Carey, S.E. Peel, E.B. Brown, R. Oberti, M. Lerotic, and J.S. Delaney (2016a) Use of multivariate analysis for synchrotron micro-XANES analysis of iron valence state in amphiboles. American Mineralogist, 101, 1171-1189, doi: 10.2183/am-2016-5556.

Dyar, M.D., M. McCanta, E. Breves, C.J. Carey, and A. Lanzirotti (2016b) Accurate predictions of iron redox state in silicate glasses: A multivariate approach using x-ray absorption spectroscopy. American Mineralogist, 101, 744-747, doi: 10.2138/am-2016-5555.

Egerton, R.F. (2011) Electron Energy-Loss Spectroscopy in the Electron Microscope, 3rd ed., 491 p., Springer, New York.

Elmaleh, A., F. Bourdelle, F. Caste, K. Benzerara, H. Leroux, and B. Devouard (2015) Formation and transformations of Fe-rich serpentines by asteroidal aqueous alteration processes: A nanoscale study of the Murray chondrite. Geochimica et Cosmochimica Acta, 158, 162-178, doi: 10.1016/j.gca.2015.03.007.

Farges, F., Y. Lefrère, S. Rossano, A. Berthereau, G. Calas, and G.E. Brown Jr (2004) The effect of redox state on the local structural environment of iron in silicate glasses: a combined XAFS spectroscopy, molecular dynamics, and bond valence study. Journal of Non-Crystalline Solids, 344, 176-188, doi: 10.1016/j.jnoncrysol.2004.07.050.

Fei, Y., D. Virgo, B.O. Mysen, Y. Wang, and H.K. Mao (1994) Temperature-dependent electron delocalization in $(Mg,Fe)SiO_3$ perovskite. American Mineralogist, 79, 826-837.

Garvie, L.A.J., A.J. Craven, and R. Brydson (1994) Use of electron-energy loss near-edge fine structure in the study of minerals. American Mineralogist, 79, 411-425.

Garvie, L.A.J., and P.R. Buseck (1998) Ratios of ferrous to ferric iron from nanometre-sized areas in minerals. Nature, 396, 667-670, doi: 10.1038/25334.

Garvie, L.A.J., T.J. Zega, P. Rez, and P.R. Buseck (2004) Nanometer-scale measurements of $Fe^{3+}/\Sigma Fe$ by electron energy-loss spectroscopy: A cautionary note. American Mineralogist, 89, 1610-1616, doi: 10.2138/am-2004-11-1204.

Golla, U., and A. Putnis (2001) Valence state mapping and quantitative electron spectroscopic imaging of exsolution in titanohematite by energy-filtered TEM. Physics and Chemistry of Minerals, 28, 119-129, doi: 10.1007/s002690000136.

Haruta, M., H. Kurata, K. Matsumoto, S. Inoue, Y. Shimakawa, and S. Isoda (2011) Local electronic structure analysis for brownmillerite Ca(Sr)$FeO_{2.5}$ using site-resolved energy-loss near-edge structures. Journal of Applied Physics, 110, 033708, doi: 10.1063/1.3610526.

Herd, C.D.K., J.J. Papike, and A.J. Brearley (2001) Oxygen fugacity of martian basalts from electron microprobe oxygen and TEM-EELS analyses of Fe-Ti oxides. American Mineralogist, 86, 1015-1024, doi: 10.2138/am-2001-8-908.

Jayasuriya, K.D., H.S.C. O'Neill, A.J. Berry, and S.J. Campbell (2004) A Mössbauer study of the oxidation state of Fe in silicate melts. American Mineralogist, 89, 1597-1609, doi: 10.2138/am-2004-11-1203.

Jiang, N., and J.C.H. Spence (2010) Electronic ionization induced atom migration in spinel $MgAl_2O_4$. Journal of Nuclear Materials, 403, 147-151, doi: 10.1016/j.jnucmat.2010.06.013.

Jiang, N., and J.C.H. Spence (2012) On the dose-rate threshold of beam damage in TEM. Ultramicroscopy, 113, 77-82, doi: 10.1016/j.ultramic.2011.11.016.

Jiang, N. (2013) Damage mechanisms in electron microscopy of insulating materials. Journal of Physics D: Applied Physics, 46, 305502, doi: 10.1088/0022-3727/46/30/305502.

Jurado-Egea, J.R., A.E. Owen, and A.K. Bandyopadhyay (1987) Electronic conduction in basalt glass and glass-ceramics - correlation with magnetite crystallization. Journal of Materials Science, 22, 3602-3606, doi: 10.1007/BF01161466.

Lauterbach, S., A.C. McCammon, P. van Aken, F. Langenhorst, and F. Seifert (2000) Mössbauer and ELNES spectroscopy of (Mg,Fe)(Si,Al)O_3 perovskite: a highly oxidised component of the lower mantle. Contributions to Mineralogy and Petrology, 138, 17-26, doi: 10.1007/pl00007658.

Le Guillou, C., H.G. Changela, and A.J. Brearley (2015) Widespread oxidized and hydrated amorphous silicates in CR chondrites matrices: Implications for alteration conditions and H_2 degassing of asteroids. Earth and Planetary Science Letters, 420, 162-173, doi: 10.1016/j.epsl.2015.02.031.

Lee, S.K., B.O. Mysen, and G.D. Cody (2003) Chemical order in mixed-cation silicate glasses and melts. Physical Review B, 68, 214206, doi: 10.1103/PhysRevB.68.214206.

Lee, S.K., G.D. Cody, and B.O. Mysen (2005) Structure and the extent of disorder in quaternary (Ca-Mg and Ca-Na) aluminosilicate glasses and melts. American Mineralogist, 90, 1393-1401, doi: 10.2138/am.2005.1843.

Lee, S.K., and C.W. Ahn (2014) Probing of 2-dimensional confinement-induced structural transitions in amorphous oxide thin film. Scientific Reports, 4, 4200, doi: 10.1038/srep04200.

Long, G.J., T. Cranshaw, and G. Longworth (1983) The ideal Mössbauer effect absorber thickness. Mössbauer Effect Reference and Data Journal, 6, 42-49.

McCartney, M.R., P.A. Crozier, J.K. Weiss, and D.J. Smith (1991) Electron-beam-induced reactions at transition-metal oxide surfaces. Vacuum, 42, 301-308, doi: 10.1016/0042-207X(91)90042-H.

Muñoz, M., V. De Andrade, O. Vidal, E. Lewin, S. Pascarelli, and J. Susini (2006) Redox and speciation micromapping using dispersive X-ray absorption spectroscopy: Application to

iron in chlorite mineral of a metamorphic rock thin section. Geochemistry Geophysics Geosystems, 7, Q11020, doi: 10.1029/2006GC001381.

Mysen, B.O., D. Virgo, and C.M. Scarfe (1980) Relations between the anionic structure and viscosity of silicate melts—a Raman spectroscopic study. American Mineralogist, 65, 690-710.

Mysen, B.O., I.S.E. Carmichael, and D. Virgo (1985) A comparison of iron redox ratios in silicate glasses determined by wet-chemical and ^{57}Fe Mössbauer resonant absorption methods. Contributions to Mineralogy and Petrology, 90, 101-106, doi: 10.1007/bf00378253.

Mysen, B.O., and P. Richet (2005) Silicate Glasses and Melts: Properties and Structure, Elsevier Inc., San Diego.

Prescher, C., F. Langenhorst, L.S. Dubrovinsky, V.B. Prakapenka, and N. Miyajima (2014) The effect of Fe spin crossovers on its partitioning behavior and oxidation state in a pyrolitic Earth's lower mantle system. Earth and Planetary Science Letters, 399, 86-91, doi: 10.1016/j.epsl.2014.05.011.

Presnall, D.C., C.L. Simmons, and H. Porath (1972) Changes in electrical conductivity of a synthetic basalt during melting. Journal of Geophysical Research, 77, 5665-5672, doi: 10.1029/JB077i029p05665.

Presnall, D.C., and N.L. Brenner (1974) A method for studying iron silicate liquids under reducing conditions with negligible iron loss. Geochimica et Cosmochimica Acta, 38, 1785-1788, doi: 10.1016/0016-7037(74)90161-6.

Roskosz, M., M.J. Toplis, D.R. Neuville, and B.O. Mysen (2008) Quantification of the kinetics of iron oxidation in silicate melts using Raman spectroscopy and assessment of the role of oxygen diffusion. American Mineralogist, 93, 1749-1759, doi: 10.2138/am.2008.2861.

Rüssel, C. (1993) Iron oxide-doped alkali-lime-silica glasses II: Voltammetric studies. Glastech. Ber., 66, 68-74.

Schmid, H.K., and W. Mader (2006) Oxidation states of Mn and Fe in various compound oxide systems. Micron, 37, 426-432, doi: 10.1016/j.micron.2005.12.004.

Smith, D.J., M.R. McCartney, and L.A. Bursill (1987) The electron-beam-induced reduction of transition metal oxide surfaces to metallic lower oxides. Ultramicroscopy, 23, 299-303, doi: 10.1016/0304-3991(87)90239-7.

Speck, A.K., A.G. Whittington, and A.M. Hofmeister (2011) Disordered silicates in space: A study of laboratory spectra of "amorphous" silicates. The Astrophysical Journal, 740, 93, doi: 10.1088/0004-637X/740/2/93.

Stebbins, J.F. (1987) Identification of multiple structural species in silicate glasses by ^{29}Si NMR. Nature, 330, 465-467, doi: 10.1038/330465a0.

Stebbins, J.F. (1988) Effects of temperature and composition on silicate glass structure and dynamics: SI-29 NMR results. Journal of Non-Crystalline Solids, 106, 359-369, doi: 10.1016/0022-3093(88)90289-X.

Stodolna, J., Z. Gainsforth, H. Leroux, A.L. Butterworth, T. Tyliszczak, D. Jacob, and A.J. Westphal (2013) Iron valence state of fine-grained material from the Jupiter family comet 81P/Wild 2 – A coordinated TEM/STEM EDS/STXM study. Geochimica et Cosmochimica Acta, 122, 1-16, doi: 10.1016/j.gca.2013.08.006.

Suzuki, S., Y. Ishikawa, M. Isshiki, and Y. Waseda (1997) Native oxide layers formed on the surface of ultra high-purity iron and copper investigated by angle resolved XPS. Materials Transactions, JIM, 38, 1004-1009, doi: 10.2320/matertrans1989.38.1004.

Tan, H., J. Verbeeck, A. Abakumov, and G. Van Tendeloo (2012) Oxidation state and chemical shift investigation in transition metal oxides by EELS. Ultramicroscopy, 116, 24-33, doi: 10.1016/j.ultramic.2012.03.002.

Thompson, M.S., T.J. Zega, P. Becerra, J.T. Keane, and S. Byrne (2016) The oxidation state of nanophase Fe particles in lunar soil: Implications for space weathering. Meteoritics & Planetary Science, 51, 1082-1095, doi: 10.1111/maps.12646.

Van Aken, P., B. Liebscher, and V. Styrsa (1998) Quantitative determination of iron oxidation states in minerals using Fe $L_{2,3}$-edge electron energy-loss near-edge structure spectroscopy. Physics and Chemistry of Minerals, 25, 323-327, doi: 10.1007/s002690050122.

Van Aken, P., and B. Liebscher (2002) Quantification of ferrous/ferric ratios in minerals: new evaluation schemes of Fe $L_{2,3}$ electron energy-loss near-edge spectra. Physics and Chemistry of Minerals, 29, 188-200, doi: 10.1007/s00269-001-0222-6.

Vargheese, K.D., A. Tandia, and J.C. Mauro (2010) Origin of dynamical heterogeneities in calcium aluminosilicate liquids. The Journal of Chemical Physics, 132, 194501, doi: 10.1063/1.3429880.

Vercamer, V., G. Lelong, H. Hijiya, Y. Kondo, L. Galoisy, and G. Calas (2015) Diluted Fe^{3+} in silicate glasses: Structural effects of Fe-redox state and matrix composition. An optical absorption and X-band/Q-band EPR study. Journal of Non-Crystalline Solids, 428, 138-145, doi: 10.1016/j.jnoncrysol.2015.08.010.

Virgo, D., B.O. Mysen, and I. Kushiro (1980) Anionic constitution of 1-atmosphere silicate melts: Implications for the structure of igneous melts. Science, 208, 1371-1373, doi: 10.1126/science.208.4450.1371.

Virgo, D., and B.O. Mysen (1985) The structural state of iron in oxidized vs. Reduced glasses at 1 atm: A ^{57}Fe Mossbauer study. Physics and Chemistry of Minerals, 12, 65-76, doi: 10.1007/BF01046829.

Weigel, C., L. Cormier, G. Calas, L. Galoisy, and D.T. Bowron (2008) Nature and distribution of iron sites in a sodium silicate glass investigated by neutron diffraction and EPSR simulation. Journal of Non-Crystalline Solids, 354, 5378-5385, doi: 10.1016/j.jnoncrysol.2008.09.030.

Williams, D.B., and B. Carter (1996) Transmission Electron Microscopy: A Textbook for Materials Science, 729 p., Springer, New York.

Zhang, Y., H. Ni, and Y. Chen (2010) Diffusion data in silicate melts. Reviews in Mineralogy and Geochemistry, 72, 311-408, doi: 10.2138/rmg.2010.72.8.

Zhang, Y., G. Yang, and Y. Yue (2013) Calorimetric signature of structural heterogeneity in a ternary silicate glass. Journal of the American Ceramic Society, 96, 3035-3037, doi: 10.1111/jace.12562.

Figure Captions

Figure 1. Fe L-edge EEL spectra from IW-basalt3 illustrating a range of oxidation states within a single sample. Gaussian fits area shown for each spectra. Fe^{2+} mostly contributes to peak 1 (P1) while peak 2 (P2) is due to Fe^{3+}; the ratio of the integrals $I_{P2}/(I_{P1}+I_{P2})$ is used to calculated the relative oxidation state Rox. San Carlos olivine ($^{[6]}Fe^{2+}$) and hematite ($^{[6]}Fe^{3+}$) are shown for comparison.

Figure 2. Quantification of data using Gaussian fits to L_3 peak, calculated from the ratio of the integral of peak 2 to the sum of peaks 1 and 2 (Rox = $I_{P2}/(I_{P1}+I_{P2})$) as illustrated in Fig. 1, plotted against $Fe^{3+}/\Sigma Fe$ for each glass determined by Mössbauer. IW and QFM samples all show a large range in oxidation states, and some spectra in all samples have higher apparent oxidation state than hematite due to Fe coordination differences.

Figure 3. Oxidation state versus **(a)** dose and **(b)** dose rate. Inset is low-dose region of (a). At high doses and dose rates, reduced areas were not seen. However, both reduced and oxidized regions were measured at low doses, indicating beam damage may contribute to, but not completely explain, highly oxidized IW- and QFM-buffered glasses. Symbols are as in Fig. 2.

Figure 4. Change in relative oxidation state (Rox) per increasing electron dose (D) plotted against thickness for repeat measurements of the exact same region. An increase in Rox in second or third scans leads to a positive value here. Matching symbols plotting at the same thickness indicate multiple measurements and often show first increasing then decreasing Rox upon additional scanning. No clear trends are seen to relate the experimental conditions or known material properties to the change in oxidation state. Symbols are as in Fig. 2.

Figure 5. High-angle annular dark field (HAADF) image of QFM-basalt6 after 60 kV acquisition of three EELS SIs in the same region-of-interest (ROI) with 0.05s/pixel dwell time

each. The rectangular mottled region where the SI was acquired shows local variation induced by the beam. The three spots in the upper right of the image are also beam damage.

Figure 6. (a) HAADF image and **(b)** EDS map from region where the beam dwelled for several seconds at 200 kV. Cations other than Si diffuse away from the spot which is ~100x the probe size. Al and Ca are concentrated in the bright rings around the beam spots relative to the other cations. **(c)** Low-loss spectrum from undamaged (black) and damaged (red) regions showing different plasmon shape and loss of Fe.

Figure 7. Oxidation state versus relative thickness shows no clear relationship. Symbols are as in Fig. 2.

Figure 8. (a) HAADF of shard from QFM-basalt6 showing lattice fringes from nano-crystalline regions with different oxidation states. **(b)** EEL spectra showing difference in shape of Fe L-edge between left and right regions of (a). **(c)** Image and **(d)** EEL spectra from QFM-basalt6. Magnetite grains are identified in the glass, having both a distinct Fe L-edge shape and rich in Fe relative to the surrounding glass. The identification of magnetite is clear in EELS O-K data also. Two small grains are clearly visualized in a map of the ratio of two different energy windows **(inset)**.

Figure 9. (a) When specific sub-regions are analyzed within single SIs, generally thinner regions are more oxidized, so that $(Rox_1\text{-}Rox_2)/(t_1\text{-}t_2)$ where $t_1 > t_2$, is negative, but the change in oxidation state with change in thickness between regions is not consistent. **(b)** Thickness of the oxidized film versus calculated initial Rox, calculated using data in (a). The thickness of the film in a single SI region is inversely related to the initial oxidation state, with thicker films forming on more reduced glass. The dotted line shows a quadratic fit to the dataset. Symbols are as in Fig. 2.

Table 1. Composition from microprobe measurements (wt%) and measured %Fe^{3+} of silicate glasses. Numbers in parentheses indicate standard deviation of measurements.

	BAS-1 (n=8)	BAS-2 (n=7)	BAS-2 (n=6)	BAS-3 (n=10)	BAS-3 (n=8)	BAS-4 (n=6)	BAS-6 (n=8)	AND-4 (n=8)	AND-4 (n=9)	RHY-2 (n=7)	RHY-3 (n=7)	RHY-3 (n=7)	RHY-5 (n=8)
f_{O2}	QFM	CO_2	QFM	QFM	IW	air	QFM	air	IW	CO_2	CO_2	IW	IW
SiO_2	49.81 (0.86)	49.42 (0.43)	49.73 (0.35)	48.42 (0.22)	51.53 (0.15)	50.96 (0.53)	51.15 (0.26)	55.61 (1.02)	61.97 (0.31)	69.35 (3.58)	70.85 (3.28)	73.21 (1.22)	71.19 (2.31)
TiO_2	1.07 (0.02)	1.60 (0.03)	1.55 (0.03)	2.84 (0.06)	2.72 (0.04)	0.82 (0.03)	2.66 (0.06)	0.66 (0.02)	0.66 (0.04)	0.33 (0.12)	0.15 (0.03)	0.28 (0.08)	0.23 (0.06)
Al_2O_3	17.94 (0.33)	15.62 (0.11)	15.51 (0.19)	17.15 (0.18)	17.90 (0.08)	17.58 (0.26)	13.79 (0.13)	18.19 (0.44)	18.10 (0.10)	17.56 (2.51)	15.81 (2.02)	16.07 (0.71)	14.39 (1.58)
FeO	7.03 (0.20)	10.56 (0.36)	9.67 (0.43)	10.85 (0.40)	11.93 (0.31)	9.96 (0.34)	10.16 (0.37)	7.62 (0.26)	7.06 (0.23)	3.29 (0.56)	1.73 (0.43)	1.83 (0.30)	3.63 (0.13)
MgO	9.14 (0.10)	7.03 (0.09)	7.10 (0.08)	5.62 (0.07)	5.77 (0.03)	6.09 (0.03)	7.10 (0.05)	4.15 (0.25)	3.78 (0.04)	0.37 (0.08)	0.25 (0.07)	0.22 (0.04)	0.04 (0.01)
CaO	10.94 (0.16)	11.60 (0.05)	11.48 (0.07)	8.97 (0.12)	9.23 (0.05)	11.35 (0.04)	11.71 (0.06)	8.14 (0.39)	7.61 (0.06)	3.19 (0.80)	1.20 (0.32)	1.09 (0.15)	0.25 (0.04)
MnO	0.01 (0.01)	0.02 (0.01)	0.01 (0.01)	0.01 (0.01)	0.01 (0.01)	0.01 (0.01)	0.01 (0.02)	0.01 (0.01)	0.01 (0.01)	0.01 (0.01)	0.00 (0.00)	0.00 (0.01)	0.01 (0.01)
Na_2O	2.96 (0.16)	2.59 (0.11)	2.66 (0.07)	3.08 (0.08)	0.68 (0.08)	2.16 (0.09)	2.30 (0.14)	3.64 (0.19)	1.01 (0.08)	5.46 (0.28)	3.76 (0.41)	3.31 (0.09)	6.07 (0.54)
K_2O	0.27 (0.02)	0.15 (0.01)	0.19 (0.02)	1.06 (0.04)	0.07 (0.02)	0.44 (0.04)	0.59 (0.03)	1.09 (0.07)	0.06 (0.01)	1.53 (0.06)	4.44 (0.26)	4.01 (0.06)	4.84 (0.16)
Total	99.15	98.60	97.89	97.99	99.84	99.35	99.46	99.11	100.25	101.09	98.18	100.03	100.65
$Fe^{3+}/\Sigma Fe$ [a]	10	80	12	22	16	89	17	100	12		71	16	30

[a] Mossbauer, error ±1-3%

Table 2. Composition of glass before and after beam damage from EDS (1σ error on counting statistics).

Wt%	**bottom spot**	**top spot**	**"un-damaged"**	**QFM-basalt3 EMPA**	**QFM-basalt3 nominal**
SiO_2	95.2(6.1)	88.3(4.1)	48.7(0.9)	48.42(0.22)	50.13
Al_2O_3	1.9(0.8)	3.4(0.6)	17.2(0.7)	17.15(0.18)	16.74
MgO	0.3(0.2)	0.00	5.8(0.3)	5.62(0.07)	5.71
CaO	0.8(0.5)	1.3(0.3)	11.2(0.5)	8.97(0.12)	8.73
FeO	0.0	0.3(0.1)	4.4(0.2) [a]	10.85(0.40)	9.07 [b]
Fe_2O_3	0.0	0.7(0.3)	9.7(0.5) [a]		2.85 [b]
Na_2O	0.0	0.0	0.0	3.08(08)	3.01
K_2O	0.0	0.0	0.0	1.06(04)	1.15
O_2 excess [c]	1.8	6.1	3.2		0.00

[a] Calculated using $Fe^{3+}/\Sigma Fe$ determined by EELS data for region.

[b] Calculated using $Fe^{3+}/\Sigma Fe$ determined by Mössbauer data for sample.

[c] Calculated based on atomic concentration and assumed stoichiometry for oxides.

Table 3. Comparison of measured volume in various techniques with commonly used spot sizes and energies.

Technique	Energy	Sample Thickness/Depth Resolution	Probe Size[a]	Interaction/ Measured Volume
ac-STEM	200 kV	20-100 nm	0.1-0.2 nm	~10^{-7} μm^3
STEM	200 kV	20-100 nm	1-5 nm	>10^{-6} μm^3
EMPA	5 kV	~0.5 μm	~1 μm	~0.5 μm^3
	25 kV	~2.5 μm	~1 μm	~5 μm^3
XANES	Hard X-ray			
GSECARS 13 ID-E		~10 μm[b]	1 μm	10 μm^3
STXM	Soft X-ray	100 nm	25 nm	6.25×10^{-5} μm^3
Raman		1-2 μm	~0.5-1 μm	1 μm^3
NanoSIMS		10 nm	50 nm	2.5×10^{-5} μm^3

[a] Before beam broadening effects

[b] Sample thickness used for XANES is strongly dependent on concentration of element of interest and geometry (fluorescence versus transmission).

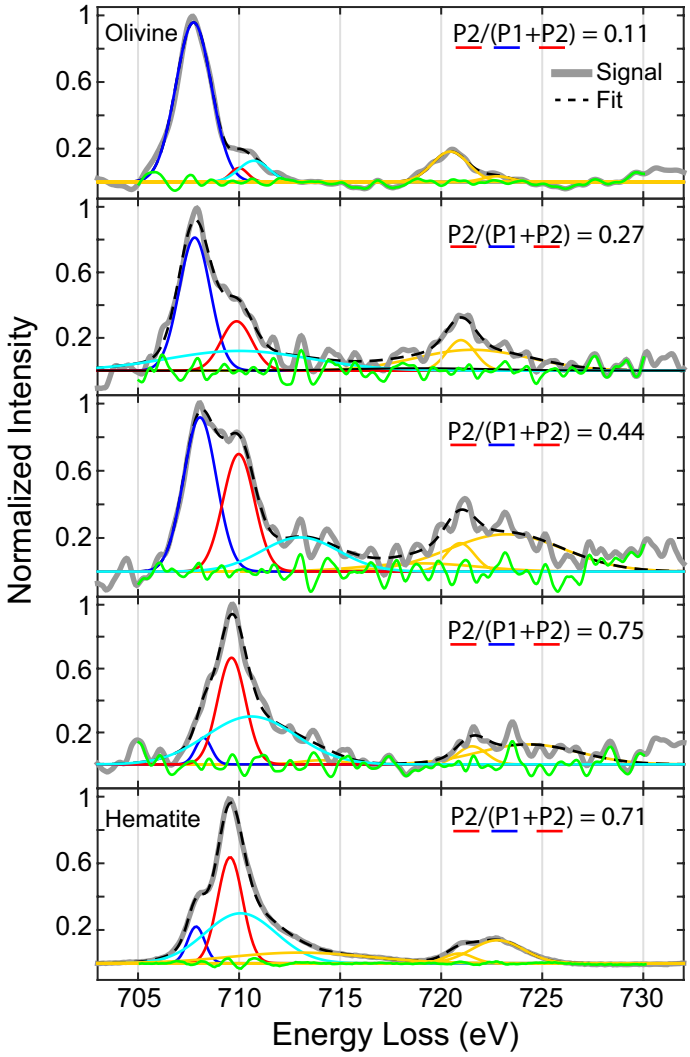

Figure 1

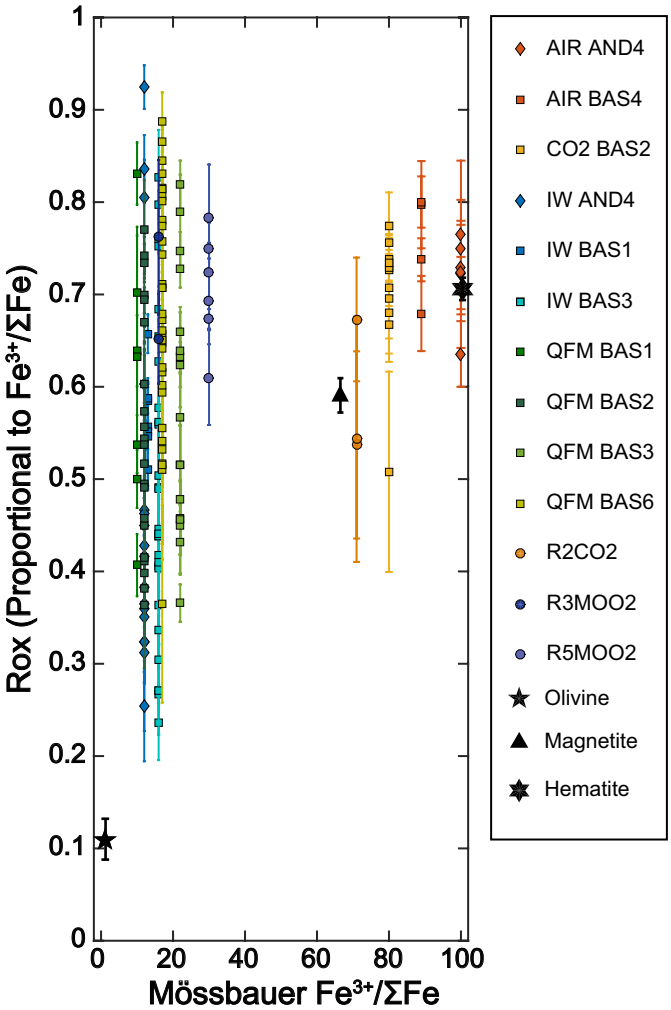
Rox (Proportional to Fe3+/ΣFe)
Mössbauer Fe3+/ΣFe
0
0.1
0.2
0.3
0.4
0.5
0.6
0.7
0.8
0.9
1
0
20
40
60
80
100
AIR AND4
AIR BAS4
CO2 BAS2
IW AND4
IW BAS1
IW BAS3
QFM BAS1
QFM BAS2
QFM BAS3
QFM BAS6
R2CO2
R3MOO2
R5MOO2
Olivine
Magnetite
Hematite

Figure 2

This is a preprint, the final version is subject to change, of the American Mineralogist (MSA)
Cite as Authors (Year) Title. American Mineralogist, in press.
(DOI will not work until issue is live.) DOI: http://dx.doi.org/10.2138/am-2016-5696

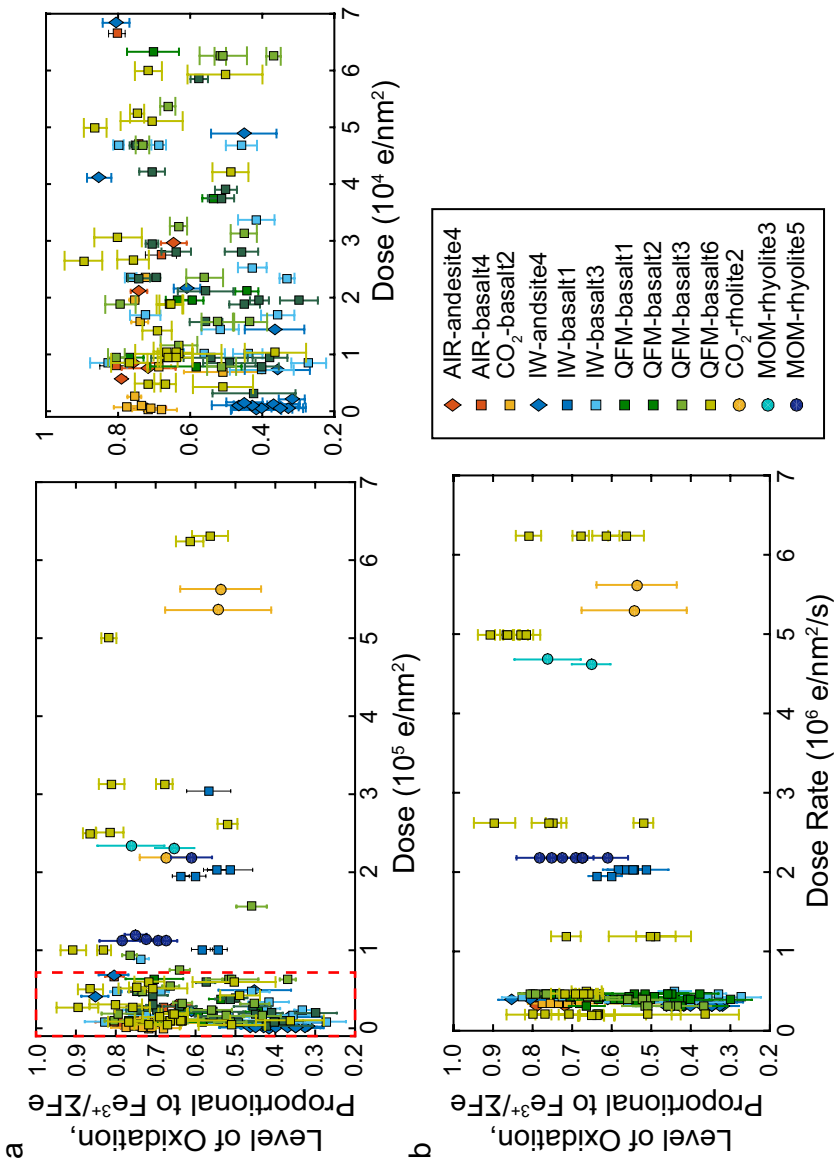

Figure 3

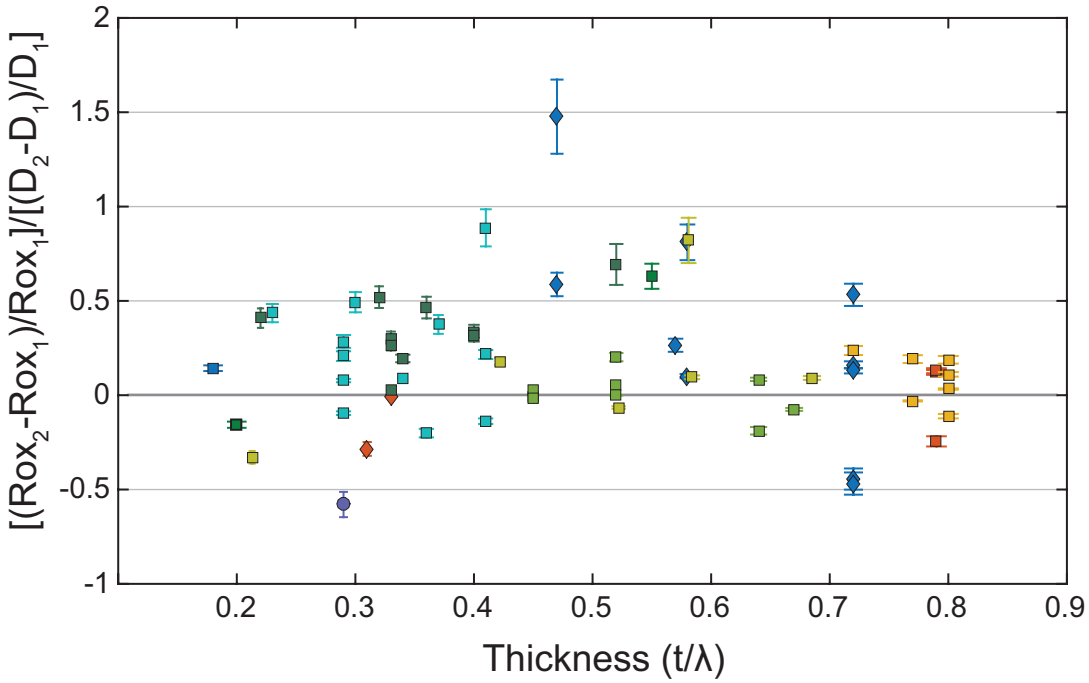
[(Rox2-Rox1)/Rox1]/[(D2-D1)/D1]
2
1.5
1
0.5
0
-0.5
-1
0.2
0.3
0.4
0.5
0.6
0.7
0.8
0.9
Thickness (t/λ)

Figure 4

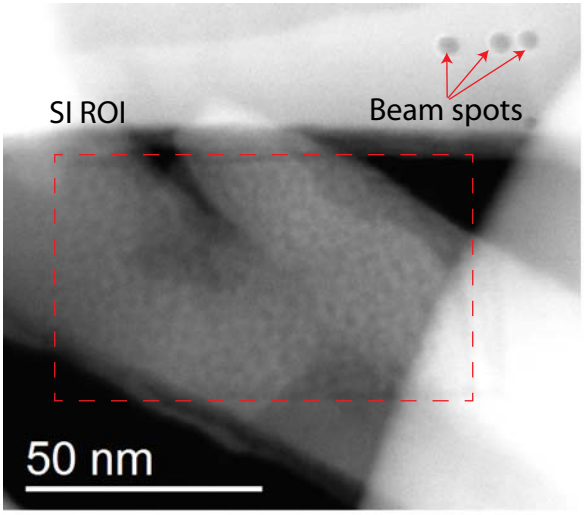

Figure 5

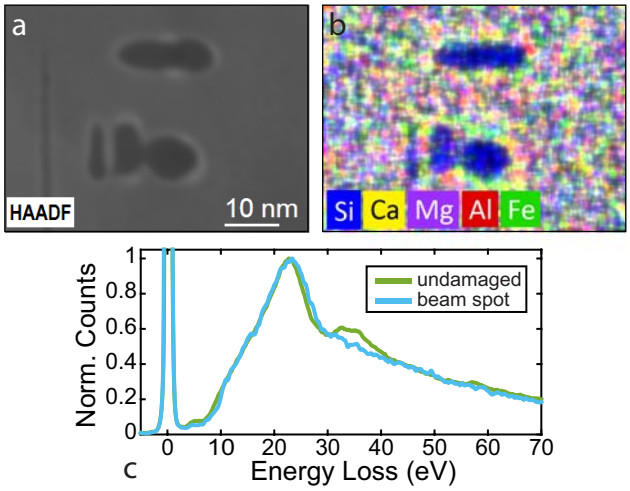
a
HAADF
10 nm
b
Si
Ca
Mg
Al
Fe
Norm. Counts
1
0.8
0.6
0.4
0.2
0
0
10
20
30
40
50
60
70
Energy Loss (eV)
undamaged
beam spot
c

Figure 6.

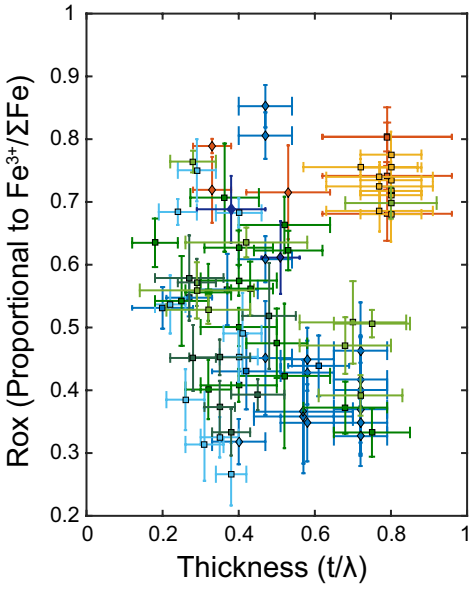
Rox (Proportional to $Fe^{3+}/\Sigma Fe$)
Thickness (t/λ)
1
0.9
0.8
0.7
0.6
0.5
0.4
0.3
0.2
0
0.2
0.4
0.6
0.8
1

Figure 7.

This is a preprint, the final version is subject to change, of the American Mineralogist (MSA)
Cite as Authors (Year) Title. American Mineralogist, in press.
(DOI will not work until issue is live.) DOI: http://dx.doi.org/10.2138/am-2016-5696

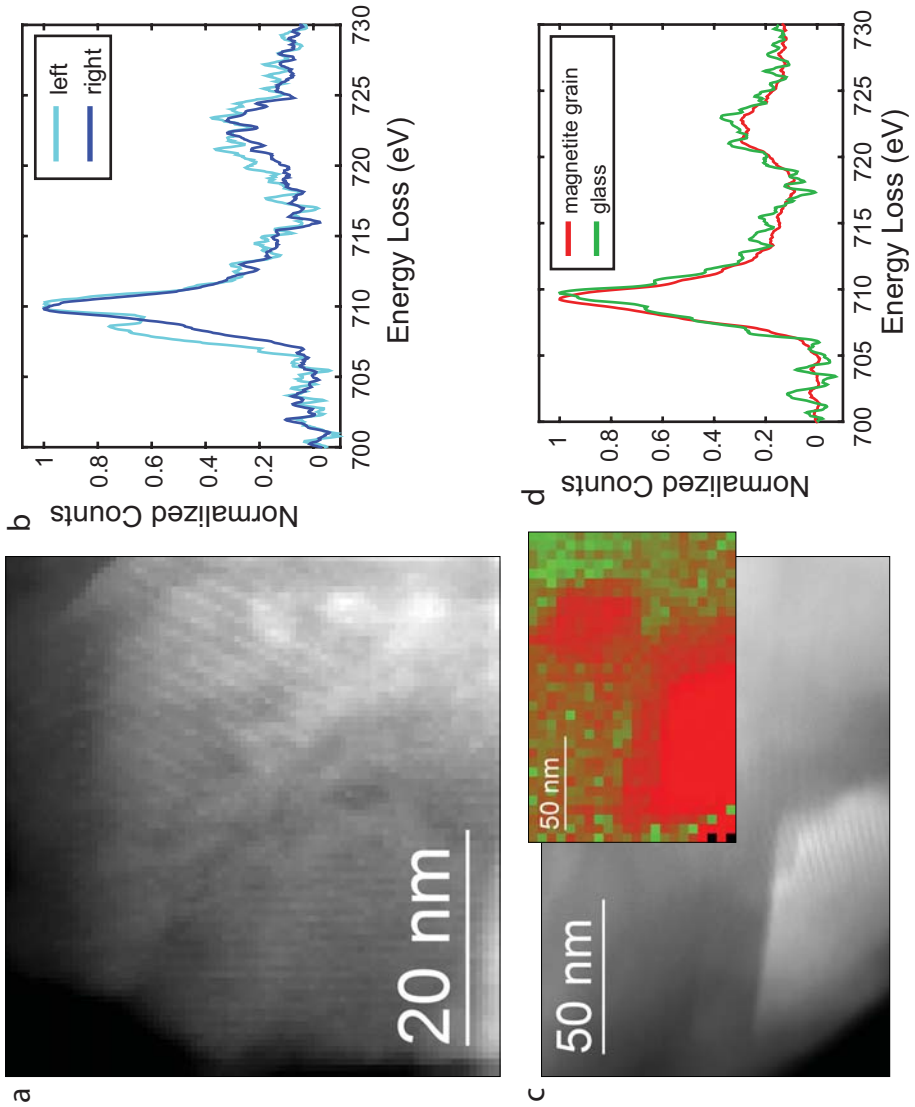

Figure 8

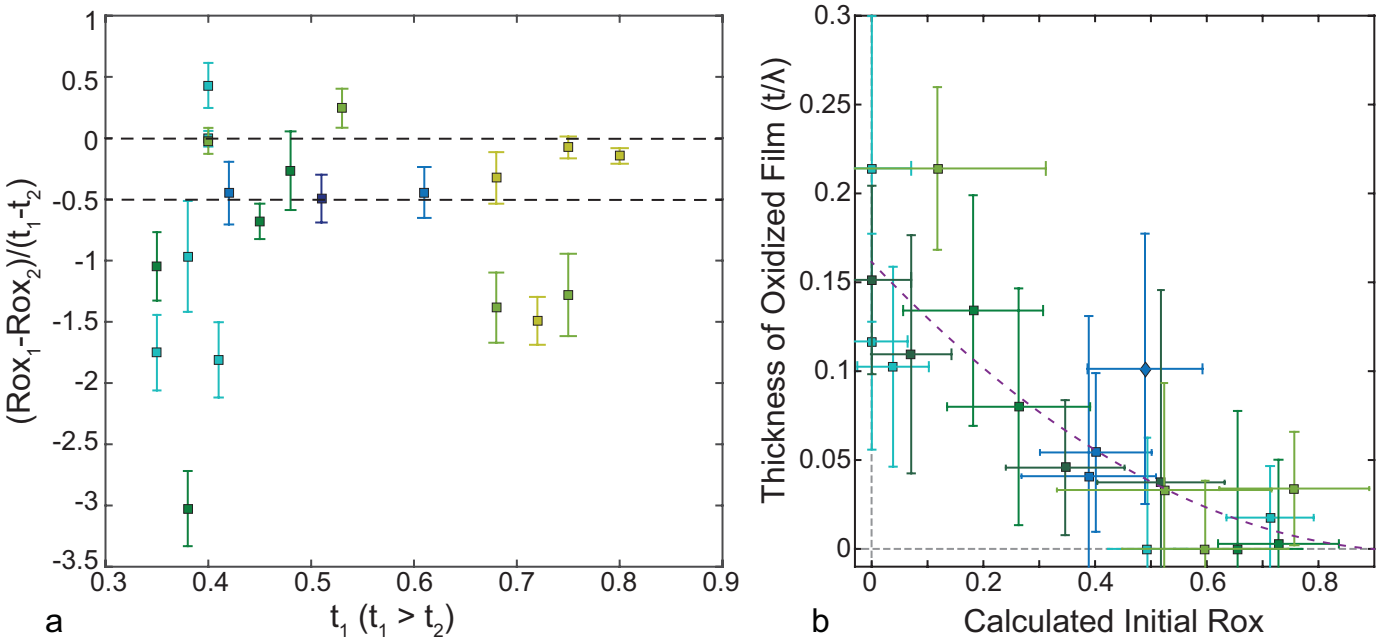
1
0.5
0
-0.5
-1
-1.5
-2
-2.5
-3
-3.5
0.3
0.4
0.5
0.6
0.7
0.8
0.9
(Rox1-Rox2)/(t1-t2)
t1 (t1 > t2)
a
0.3
0.25
0.2
0.15
0.1
0.05
0
0
0.2
0.4
0.6
0.8
Thickness of Oxidized Film (t/λ)
Calculated Initial Rox
b

Figure 9